Materials Characterization 165 (2020) 110377

Contents lists available at ScienceDirect

Materials Characterization

journal homepage: www.elsevier.com/locate/matchar

Fabrication of high-strength Mg-Gd-Zn-Zr alloy via selective laser melting

Qingchen Deng[a], Yujuan Wu[a,b,c,*], Yuanhang Luo[a], Ning Su[a], Xiaoyu Xue[a], Zhiyu Chang[a], Qianye Wu[a], Yanting Xue[a], Liming Peng[a,b,c]

[a] National Engineering Research Center of Light Alloy Net Forming and State Key Laboratory of Metal Matrix Composites, School of Materials Science and Engineering, Shanghai Jiao Tong University, Shanghai 200240, China
[b] Shanghai Light Alloy Net Forming National Engineering Research Center Co., Ltd., Shanghai 201615, China
[c] Shanghai Innovation Institute for Materials, Shanghai 200444, China

ARTICLE INFO

Keywords:
Selective laser melting
Mg-Gd-Zn-Zr alloy
Formability
Element vaporization
Microstructure
Tensile properties

ABSTRACT

A Mg-11.00Gd-1.77Zn-0.43Zr (wt.%) alloy named GZ112K was prepared by selective laser melting (SLM) with different processing parameters. The formability, element vaporization, microstructure and tensile properties of the SLMed samples at different scanning speed and hatch spacing were characterized. The process map at a constant laser power of 80 W for the alloy has been established. It shows that the optimum scanning speed and hatch spacing are 300–700 mm/s and 100 μm respectively. The SLMed samples have fine grains of about 2 μm and dispersed eutectic phase of β-$(Mg,Zn)_3Gd$ due to the very high cooling rate, high solid solubility of Gd and Zn elements in α-Mg matrix owing to the effect of solute trapping. The SLMed GZ112K alloy with scanning speed of 300 mm/s and hatch spacing of 100 μm has yield strength (YS) of 325 MPa, ultimate tensile strength (UTS) of 332 MPa and elongation of 4.0% at room temperature. Compared with as-cast alloy, the SLMed GZ112K alloy has much higher YS (+162 MPa), UTS (+122 MPa) and comparable elongation (+0.4%).

1. Introduction

Magnesium (Mg) alloys are one of the most promising structural materials in automobile, aircraft, electronic consumer industries and medical industries because of their low density, high specific strength, good damping capacity, excellent biocompatibility and biodegradability [1]. Mg-Gd based alloys display very high strength due to the strong precipitation hardening effect of Gd [2]. Besides, the minor addition of Zn element can improve the strength and plasticity simultaneously by introducing basal γ′ precipitates and long period stacking ordered (LPSO) structure [3,4]. Furthermore, Zr element can refine the grains through promoting nucleation as heterogeneous nucleation cores during solidification [5]. Rong et al. [6] reported a high-strength casting Mg-15Gd-1Zn-0.4Zr (wt%) alloy with UTS above 400 MPa, which was attributed to combined strengthening and toughening effect of the composite β′ and γ′ precipitates.

Nowadays Mg alloys are mainly fabricated by casting method such as sand casting [7], permanent mold casting [6] and die casting [8], which suffer from the problems of casting defects, poor mechanical properties, long manufacturing cycles and low dimensional accuracy and incapable of fabricating very complex structures [9]. In order to further expand the applications of Mg alloys, new manufacturing methods are urgently needed to be developed. Selective laser melting (SLM) is a rapid manufacturing technology which can build complex geometric shaped parts layer by layer according to CAD model without any molds in a relatively short cycle [10]. Highly focused laser energy and extremely short interaction time between the laser beam and the powder bed result in a small molten pool and very high cooling rate of approximately 10^5 K/s [11], which leads to a fine-grained microstructure with remarkable mechanical properties. Fine grain strengthening can increase both strength and plasticity especially for Mg alloys containing very high Hall-Petch coefficient [12], so selective laser-melted structural components usually exhibit better mechanical properties than conventionally cast or even forged components [13–15].

SLM has been successfully applied to manufacture iron-based alloys [16], Ni alloys [17], Ti alloys [18] and Al alloys [19], etc. However, researches on SLM of Mg and its alloys are still in infancy owing to low boiling points, high vapor pressure and high affinity for oxygen [20]. Until now, only a few researches on SLM of pure Mg [13,21], Mg-Al series [14,22–28], Mg-Zn series [29–32], Mg-Ca series [33] and WE43 [10,15] have been reported focusing on optimization of processing parameters for high density, mechanism of element evaporation,

* Corresponding author at: National Engineering Research Center of Light Alloy Net Forming and State Key Laboratory of Metal Matrix Composites, School of Materials Science and Engineering, Shanghai Jiao Tong University, Shanghai 200240, China.
E-mail address: wuyj@sjtu.edu.cn (Y. Wu).

https://doi.org/10.1016/j.matchar.2020.110377
Received 14 January 2020; Received in revised form 8 May 2020; Accepted 8 May 2020
Available online 19 May 2020

fabrication of porous implants for biomedical applications, adjustment of the unique SLMed microstructures and corresponding performances. An extremely fine, homogeneous microstructure with grain sizes of ~1 μm and very fine secondary phases was reported in SLMed WE43 alloy [15], which contributes to excellent tensile properties: YS of 296 MPa, UTS of 308 MPa and elongation of 11.9%. It seems that the very high cooling rate of SLM in an order of 10^5 K/s leads to such a fine and homogeneous microstructure and excellent tensile properties. As reported, no SLM research was carried out on Mg-Gd based alloys, which exhibit better mechanical properties than the alloy systems reported above. Therefore, the combination of high cooling rate of SLM technology and high strength of Mg-Gd based alloys in order to fabricate high-strength and complex-shaped components is of great significance to more applications of Mg alloys.

In the present study, Mg-11.00Gd-1.77Zn-0.43Zr (wt%) alloy samples were fabricated by SLM with different processing parameters and their microstructure and tensile properties at room temperature were systematically investigated and compared with semi-continuous casting samples. Optimum processing parameters for the alloy have been obtained to get remarkable tensile properties. The 'processing parameters-microstructure-tensile properties behavior' relationship of SLMed GZ112K alloys was established.

2. Experimental details

2.1. Materials preparation

Spherical powders of the GZ112K alloy (Tangshan Weihao Magnesium Powder Co., LTD, China) were manufactured from re-melting semi-continuous casting ingots and using gas atomization process. A part of the semi-continuous casting ingots was used to determine the microstructure and the tensile properties of the as-cast state.

The actual chemical compositions of the as-cast material, the original powder and the SLMed materials under different processing parameters were determined by an inductively coupled plasma atomic emission spectroscopy analyzer (ICPAES, Perkin-Elmer, Optima™ 7300 DV). The chemical composition of the GZ112K powders is listed in Table 1. The measured chemical composition of the powders is as follows: the contents of Gd, Zn and Zr are 11.00 ± 0.26 wt%, 1.77 ± 0.07 wt% and 0.43 ± 0.02 wt%, which are close to the nominal compositions (Mg-11Gd-2.0Zn-0.4Zr). Besides, the oxygen content of the powder measured by oxygen nitrogen hydrogen analyzer is very low, only 0.008 wt%.

Fig. 1 shows the morphology, particle size distribution and XRD patterns of the GZ112K powders. A small number of satellite powders and wrapped powders can be seen from Fig. 1a. The D10, D50, D90 and mean particle sizes of the powders are 30.88, 41.59, 59.45 and 43.94 μm respectively, as presented by the particle size distribution shown in Fig. 1c. As shown in Fig. 1b and d, the powders are composed of α-Mg matrix, β-$(Mg,Zn)_3Gd$ eutectic phase and γ′ precipitates. The nano-sized γ′ precipitates will be identified in Fig. 9. Besides, SLMed samples have the same phase composition as powders.

2.2. Processing

All samples were deposited by a commercial ZRapid iSLM 150 machine (ZRapid Tech Co., LTD, China) with IPG fiber laser of 200 W according to the designed processing parameters shown in Fig. 2a. Before SLM process, the powder was preheated in a vacuum oven at 180 °C for 2 h and the substrate plate of GW83K alloy was sand-blasted. The inlet and outlet of inert gas (Fig. 2b) are located on the side of the substrate plate to remove the large quantities of fumes caused by the serious evaporation of Mg. Square blocks with a size of 10 × 10 × 10 mm^3 were built for microstructure observation and bone-shaped samples with gauge dimensions of 18 × 3 × 10 mm^3 were prepared for tensile tests. Square blocks were scanned with strip strategy (Fig. 2d) containing long bidirectional vectors [34] and the raster changing angle between two neighboring layers (hatch angle θ) [35] was 0° in order to get a neatly arranged molten pool for observing the microstructure characteristics. Bone-shaped samples were scanned with island strategy (Fig. 2e) and the hatch angle was 73° for the purpose of weakening the anisotropy of microstructure and avoiding stress concentration. The size of an island is 5 × 5 mm^2 and the overlapping width of adjacent small islands is 0.2 mm so as to increase the density of samples. The sequence of laser processing of different islands is: ① → ② → ③ → ④, which is beneficial to obtaining a uniform temperature field in the SLMed samples.

2.3. Microstructure characterization and tensile tests

Following SLM process, all samples were separated from the substrate plate using electric discharge wire cutting and bone-shaped samples were cut into pieces with thickness of 1.5 mm for tensile tests (Fig. 2c).

After being mechanical ground and polished, the specimens were etched in the acetic-picral solution (4.2 g picric acid, 10 ml acetic acid, 80 ml ethyl alcohol and 10 ml water) for microstructure observations with an optical microscope (OM, Zeiss Axio observer) and a scanning electron microscope (SEM, TESCAN MIRA3 equipped with a back-scatter electron (BSE) detector, an energy dispersive X-ray spectrometer (EDS, Aztec X-Max N80)). Samples for electron backscatter diffraction (EBSD) were prepared by mechanical grinding and then using SiC abrasive paper (#1200, #2400, #4000), diamond suspension (6 μm, 3 μm, 1 μm) and OPS suspension one by one to polish. EBSD mapping was performed on a TESCAN GAIA3 field-emission scanning electron microscope equipped with an Oxford Aztec Nordlys Max3 EBSD system. The specific parameters of mapping are as follows: the step size is 0.2 μm, the acceleration voltage is 20 kV, the working distance is 15 mm and the tilt angle of the sample stage is 70°. The TSL OIM Analysis 7 software was used to generate grain orientation maps. The grain size was measured by linear intercept method according to the ASTM E112-12, in which each value was the average of at least five statistics. Thin foil specimens for transmission electron microscope (TEM) observation were prepared by the following steps: Firstly, tiny discs with 3 mm diameter were punched from a 0.5 mm thickness thin slice of alloy followed by mechanical ground to 50 μm thickness foil. Secondly, the central regions of discs were pre-thinned to 30 μm using

Table 1
The actual chemical compositions of the as-cast material, the original powder and the SLMed materials under different processing parameters (wt%).

Material	Gd	Zn	Zr	Mg	Mg + Zn	Mg/Zn
As-cast	11.93 ± 0.29	1.94 ± 0.09	0.41 ± 0.03	85.72 ± 0.31	–	–
Powder	11.00 ± 0.26	1.77 ± 0.07	0.43 ± 0.02	86.80 ± 0.27	88.57	49.04
SLMed-V100HS100	12.64 ± 0.24	1.52 ± 0.10	0.57 ± 0.04	85.27 ± 0.26	86.79	56.10
SLMed-V500HS50	12.23 ± 0.28	1.61 ± 0.06	0.52 ± 0.01	85.64 ± 0.29	87.25	53.19
SLMed-V500HS100	11.89 ± 0.15	1.69 ± 0.05	0.49 ± 0.02	85.93 ± 0.16	87.62	50.85
SLMed-V500HS150	11.45 ± 0.18	1.72 ± 0.04	0.46 ± 0.01	86.37 ± 0.18	88.09	50.22
SLMed-V1000HS100	11.08 ± 0.23	1.75 ± 0.08	0.44 ± 0.02	86.73 ± 0.24	88.48	49.56

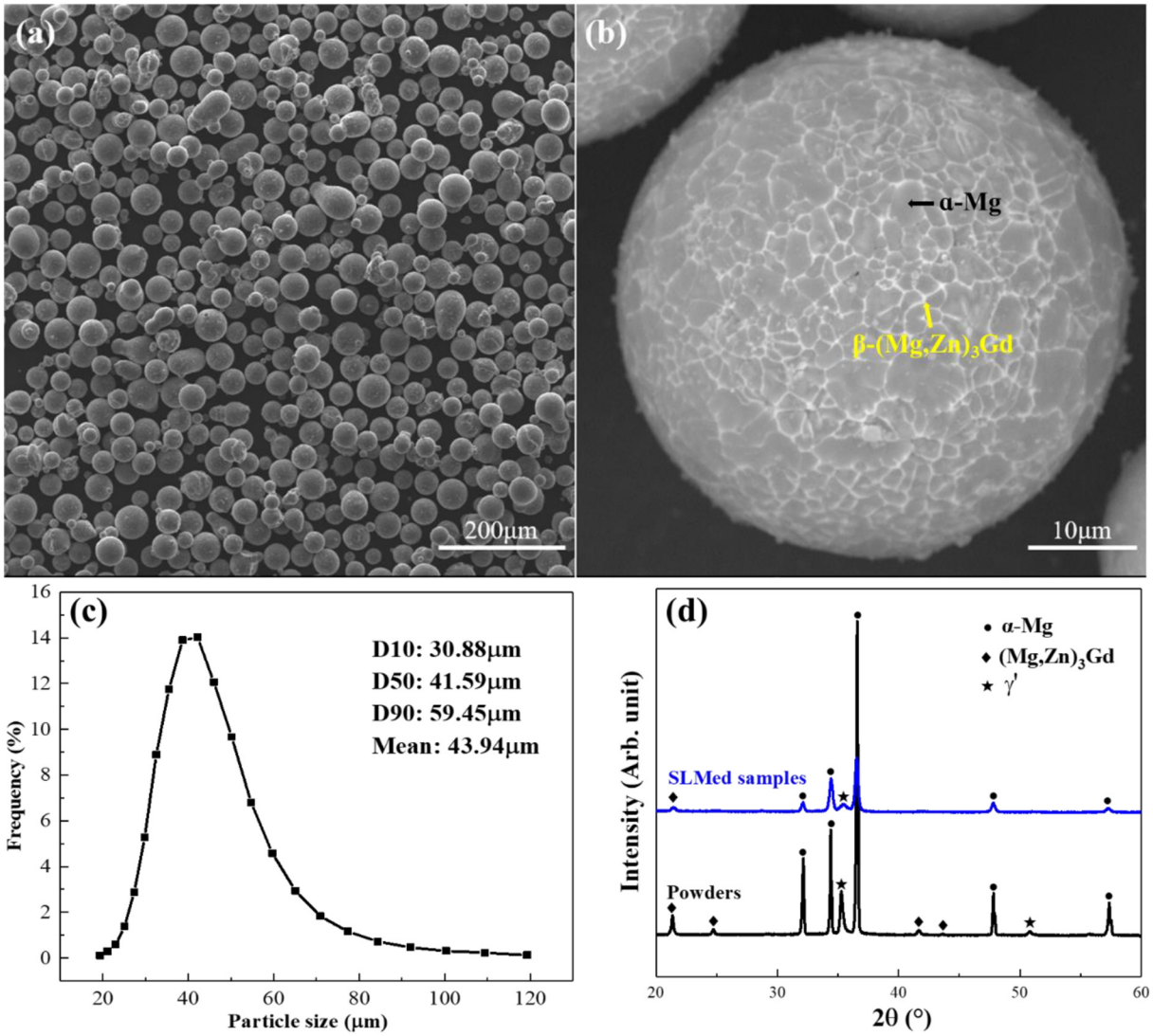

Fig. 1. The morphology (a. low magnification; b. high magnification), particle size distribution (c) and X-ray diffraction (XRD) patterns (d) of GZ112K powders.

Dimple Grinder II. Finally, the discs were polished by the Precision ion polishing system (PIPs 695, 6° under 6 keV until perforation followed by 3° under 3 keV for 10 min, 3° under 1 keV for 10 min and 2° under 0.5 keV for 10 min to expand the thin area).TEM observations were performed on FEI TECNAI G^2 S-TWIN with an energy dispersive X-ray spectrometer (EDS) operating at 200 kV to examine the microstructure of the precipitates and the chemical composition in α-Mg matrix. Tensile tests were carried out on a Zwick/Roell Z100 material test machine with a constant loading speed of 0.5 mm/min. The loading direction of the tensile tests is perpendicular to the building direction of SLM process.

3. Results and discussion

3.1. Formability

During SLM experiments, 18 square blocks were prepared using different scanning speed and hatch spacing to optimize the SLM processing parameters for the alloy. A process map based on laser energy density and defect features on OM images (Fig. 4) was then established, as shown in Fig. 3. Laser energy density (J/mm^3) is defined as laser energy per unit volume called volume energy density, which can be calculated by the following Eq. (1):

$$E_v = \frac{P}{V \bullet HS \bullet t} \quad (1)$$

where P is laser power (W), V is scanning speed (mm/s), HS is hath spacing between adjacent laser scanning tracks (mm), t is layer thickness (mm). Process map is divided into three zones according to different microstructure characteristics.

(I) High energy input zones (pores defects): the laser energy density is extremely high in this zone owing to very low scanning speed. High energy input increases the temperature in the molten pool, which contributes to the serious vaporization of Mg powders. Besides, the depth of molten pool is much larger than the width resulting in a keyhole mode SLM condition [36]. As result, a large number of circular pores defects appears in the bottom of molten pool (Fig. 4a) due to a keyhole collapse and the Mg vapor in the bottom of the molten pool not having sufficient time to float up and escape before the surrounding melt had solidified [28].

(II) Medium energy input zones (forming zones): thanks to appropriate scanning speed (300–700 mm/s) and hatch spacing (50–100 μm), samples without obvious defects can be obtained. It can be seen from Fig. 4b that fish-scale-shaped molten pool are arranged neatly.

(III) Low energy input zones (lack of fusion defects): high scanning

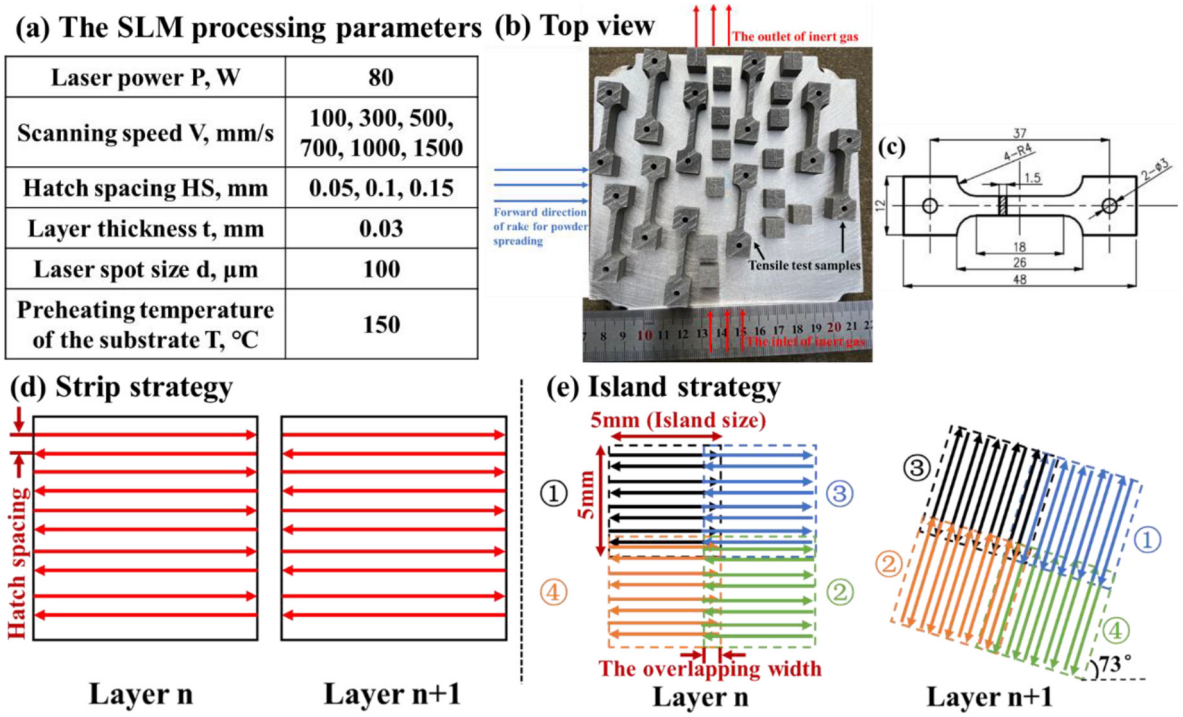

Fig. 2. Experiment details of this study: (a) the SLM processing parameters used in the experiment; (b) top view of SLMed samples; (c) the dimensions of the tensile test samples; (d) schematic representation of the strip strategy; (e) schematic representation of the island strategy.

speed and hatch spacing results in low laser energy density. Numerous lack of fusion defects (Fig. 4c) occur between adjacent scan tracks and layers owing to the molten pool overlapping insufficiently and not enough heat input of laser.

The relative density of SLMed GZ112K samples was measured by counting the area percentage of defects (pores and lack of fusion) in tested sections in order to further comprehend how processing parameters (scanning speed and hatch spacing) influence formability. The relative density of each sample was determined by at least five statistics. Fig. 5 gives the relationship between the relative density and processing parameters. There is a general decreasing trend of the relative density with increasing scanning speed (Fig. 5a) except for the lowest scanning speed of 100 mm/s leads to many pores. The relative density of SLMed GZ112K samples in forming zones (300–700 mm/s) is highest, which is consistent with the results of Figs. 3 and 4. At a fixed scanning speed of 500 mm/s, the sample with a hatch spacing of 100 μm has the highest relative density (Fig. 5b) and the reason for this will be discussed in Fig. 15. In the present study, the highest relative density of SLMed GZ112K sample is 99.95 ± 0.03% at scanning speed of 300 mm/s and hatch spacing of 100 μm. The relative density has a significant effect on room-temperature tensile properties, which will be discussed in the Section 3.3.

3.2. Element vaporization

Table 1 lists the chemical compositions of SLMed materials under different processing parameters. Compared with original powder, all SLMed materials have higher content of Gd and Zr and lower content of Zn and Mg. With the increase of laser volume energy density, the content of Gd and Zr increases and the content of Zn and Mg decreases. According to Langmuir model [37], the vaporization rate of an element can be predicted by the following Eq. (2):

$$J_i = 4.375 \times 10^{-4} \cdot \gamma_i \cdot X_i \cdot P_i^0 \cdot \left(\frac{M_i}{T}\right)^{1/2} \quad (2)$$

where J_i is the vaporization rate of element i ($g \cdot cm^{-2} \cdot s^{-1}$), γ_i is the activity of element i in the alloy, X_i is the molar fraction of element i in

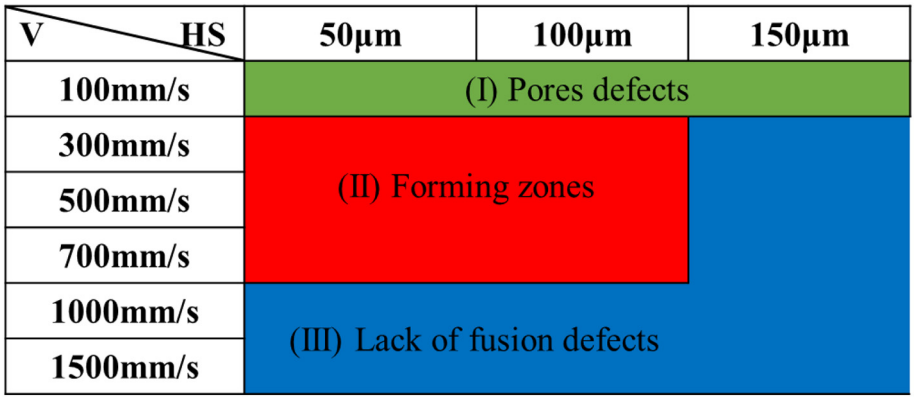

Fig. 3. Process map at a constant laser power of 80 W for GZ112K alloy, results as function of the range of laser scanning speed and hatch spacing.

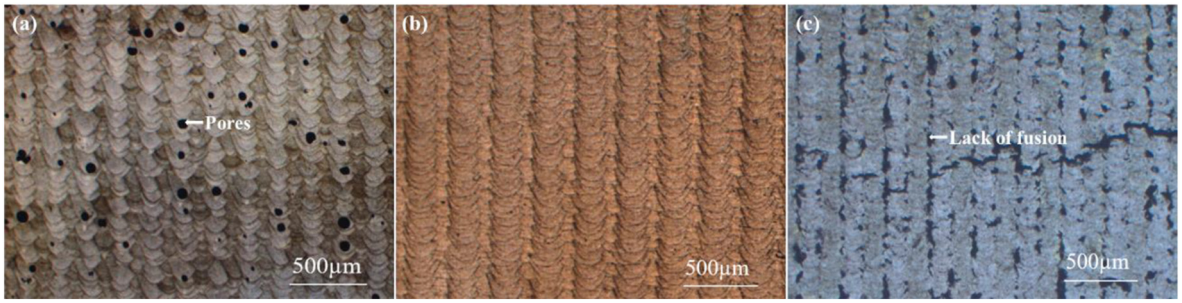

Fig. 4. OM images of the SLMed GZ112K alloys corresponding to three different processing zones: (a) pores defects; (b) forming zones; (c) lack of fusion defects.

the alloy, P_i^0 is the standard pressure of pure element i (*Pa*), M_i is the molecular weight of element i (g/mol) and T is the absolute temperature (K). Fig. 6 shows the vaporization rate of Mg and the alloying elements ratios in GZ112K molten pool under various temperatures (the inner graph in Fig. 6a is the magnified curve in the temperature range of 923 K to 1100 K). The vaporization rate of Mg element (J_{Mg}) increases rapidly as the temperature of the molten pool increases (Fig. 6a). In the temperature range of 923 K (melting point of pure Mg) to 2000 K, J_{Mg} are 8.2 × 10^6–2.0 × 10^{14} times, 7.9–20.8 times, and 5.4 × 10^{12}–1.6 × 10^{27} times of J_{Gd}, J_{Zn}, and J_{Zr}, respectively (Fig. 6b–d). Therefore, compared with the vaporization rate of Mg, the vaporization rates of Gd and Zr are very small. Considering the weight fraction of Mg is 49 times of Zn in original powder, so the vaporization of Zn is more intense than Mg owing to higher vapor pressure of Zn. A greater relative vaporization of Zn contributes to a higher Mg/Zn ratio than original powder. As laser volume energy density increases, the temperature of the molten pool increases and more time for Mg and Zn elements to vaporize from the liquid surface, causing the vaporization of Mg and Zn to become more intense, so the total content of Mg and Zn decreases and Mg/Zn ratio increases. In conclusion, element vaporization mainly targeted at Mg and Zn during the process of SLM.

3.3. Microstructure characterization

Fig. 7 presents the OM and SEM images of semi-continuous as-cast alloy and the SLMed GZ112K alloy (V = 300 mm/s, HS = 100 μm). The microstructure of SLMed GZ112K alloy is quite different from the conventional as-cast alloy. The grain size of SLMed samples (Fig. 7c–d) is significantly smaller than the as-cast samples (Fig. 7a–b) and the eutectic β-$(Mg,Zn)_3Gd$ phase becomes lesser and thinner, both of which have a beneficial effect on mechanical properties. It is attributed to that SLM owns very high cooling rate of approximately 10^5 K/s [11] while the cooling rate of traditional semi-continuous casting is only about 10 K/s [38]. What's more, there is a slight difference between the grains inside and outside the molten pool. The grains at the molten pool boundary (Fig. 7c–d) are the finest due to the highest cooling rate. In general, the SLMed GZ112K alloy has uniform and extremely fine equiaxed grains, which is quite different from those of SLMed iron-based [16], Ni [17], Ti [18] and Al [19] alloys that usually have coarse columnar grains growing parallel to building direction. According to the interdependence theory [39], the growth restriction factor Q of the alloy determines the rate of development of a constitutional supercooling zone during solidification. The SLMed alloys containing high Q values are usually easier to form equiaxed grains rather than columnar grains [40]. Zr is a commonly used grain refinement element in Mg alloys with a high Q value of 38.29 [41]. Thanks to sufficient Zr element content in the original GZ112K alloy powder, the SLMed GZ112K alloys are consist of uniform equiaxed grains.

Fig. 8 shows the EBSD orientation map (a), grain size distribution (b), (0001) pole figures (c) and inverse pole figures (d) of the SLMed GZ112K alloy (V = 300 mm/s, HS = 100 μm). As shown in Fig. 8a, the fine equiaxed grains are randomly oriented in various crystal orientations and the average grain size is only 1.53 ± 0.72 μm (Fig. 8b). The cooling rate decreases from molten pool boundary to the center, so the grain size of the left top corner (Fig. 8a) near the center of molten pool is a little larger than other regions. What's more, the SLMed GZ112K alloy displays weak textures because of fine equiaxed grains and the maximum intensity of texture from (0001) pole figures (Fig. 8c) and inverse pole figures (Fig. 8d) are only 3.073 and 1.714 respectively.

Fig. 9 shows bright-field TEM micrographs and corresponding SAED patterns of the SLMed GZ112K alloy (V = 300 mm/s, HS = 100 μm). The SLMed GZ112K alloy consisted of uniform and fine equiaxed grains (Fig. 9a), and basal precipitates, which were identified to be the γ′ precipitates reported by Rong et al. in Mg-Gd-Zn alloys [6,42] were

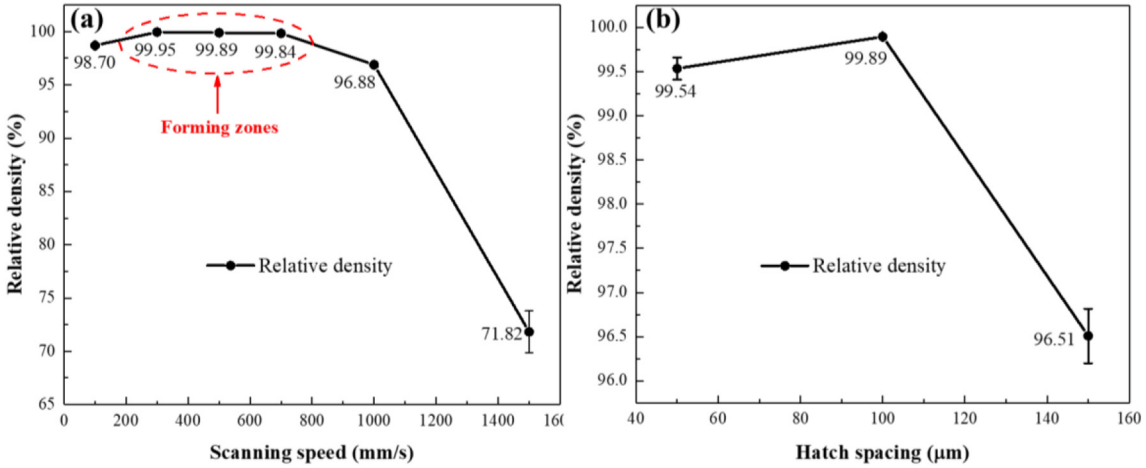

Fig. 5. Effect of (a) scanning speed (the hatch spacing is fixed at 100 μm) and (b) hatch spacing (the scanning speed is fixed at 500 mm/s) on the relative density of SLMed samples.

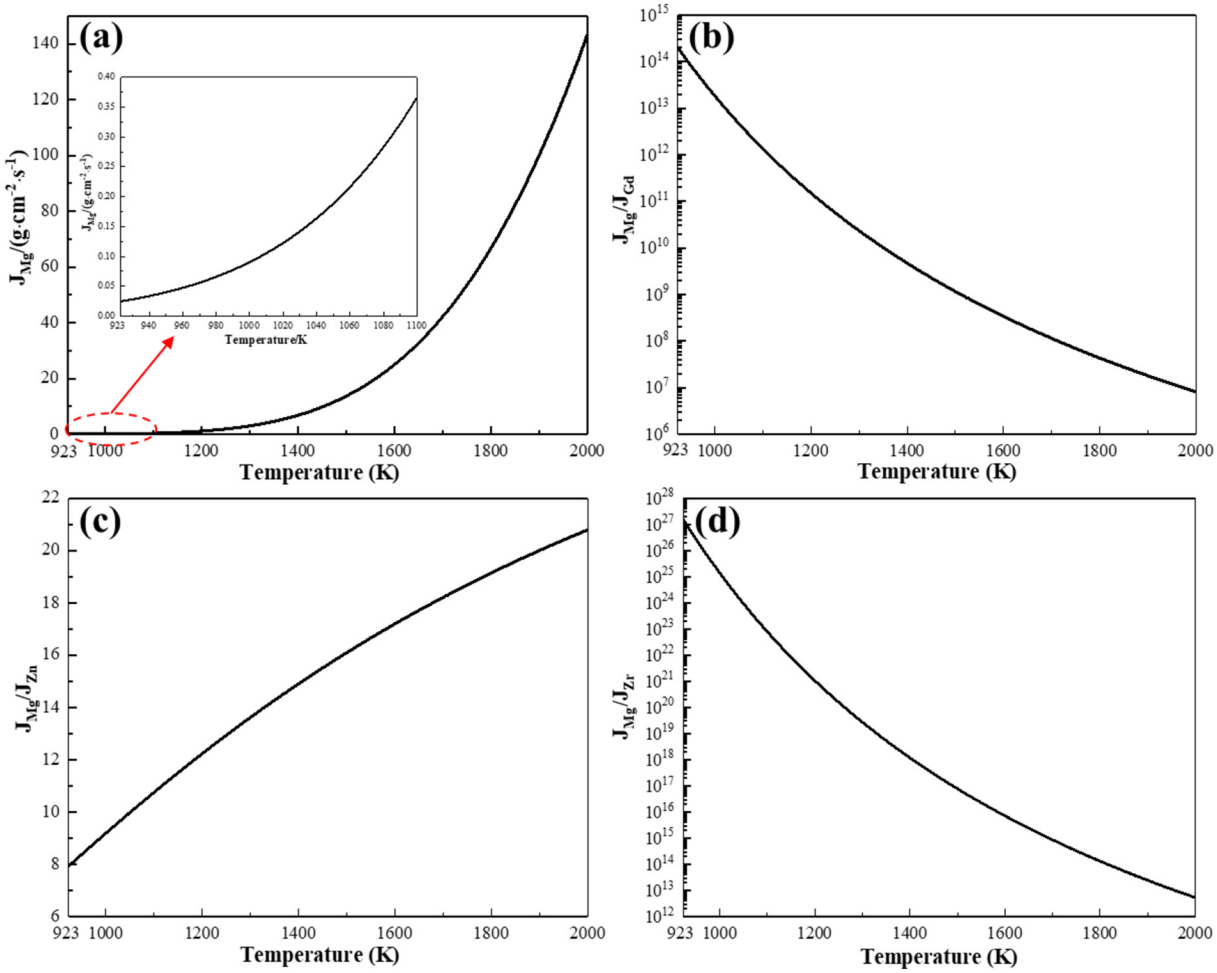

Fig. 6. The vaporization rate of Mg and the alloying elements ratios in GZ112K molten pool under various temperatures (J_{Mg}, J_{Gd}, J_{Zn} and J_{Zr} represent the vaporization rate of Mg, Gd, Zn and Zr): (a) J_{Mg}; (b) J_{Mg}/J_{Gd}; (c) J_{Mg}/J_{Zn}; (d) J_{Mg}/J_{Zr}. The inner graph in panel a is the magnified curve in the temperature range of 923 K to 1100 K.

found inside some grains (Fig. 9b). Compared with a 14H-type LPSO structure reported in an as-cast Mg-Gd-Zn-Zr alloy during conventional ingot metallurgy [43], there was no LPSO structure in the SLMed GZ112K alloy due to the very high solidification rate during SLM process. However, basal γ′ precipitates are the building block of 14H-type LPSO structure and they might transform into 14H-type LPSO structure during the post heat treatments.

Fig. 10 gives SEM images of the SLMed GZ112K alloys at different scanning speeds. By counting the average grain size and the area fraction of eutectic β-$(Mg,Zn)_3Gd$ phase of semi-continuous as-cast alloy and SLMed GZ112K alloys at different scanning speeds, it can be seen from Fig. 11 that the average grain size and the area fraction of eutectic β-$(Mg,Zn)_3Gd$ phase of semi-continuous as-cast alloy are 37.9 ± 2.6 μm and 7.3 ± 0.6% respectively, while the average grain size and the area fraction of eutectic β-$(Mg,Zn)_3Gd$ phase of SLMed GZ112K alloy at scanning speed of 100 mm/s are only 2.34 ± 1.02 μm and 3.8 ± 0.04%. More specifically, the average grain size is reduced by 93.8% and the area fraction of eutectic β-$(Mg,Zn)_3Gd$ phase is reduced by 47.9%. Evidently, the higher the scanning speed, the smaller the average grain size. This was attributed to the difference in solidification and cooling rates. The temperature during laser melting usually decreases with increasing scanning speed leading to higher solidification and cooling rates. The higher the solidification and cooling rates, the shorter the time available for grain coarsening. Therefore, increasing scanning speed would result in grain refinement. What's more, the area fraction of eutectic β-$(Mg,Zn)_3Gd$ phase become smaller with increasing scanning speed. This phenomenon may be attributed to two reasons. Firstly, higher scanning speed reduces the vaporization effect of Mg element and then β-$(Mg,Zn)_3Gd$ phase which is enrichment of Gd become less with decreasing content of Gd (Table 1). Secondly, the effect of solute trapping [44] during rapid solidification plays an important in determining the final content of β-$(Mg,Zn)_3Gd$ phase. Based on the model for solute redistribution during continuous growth, solute distribution coefficient of the moving solid–liquid phase interface (k') can be expressed by the following Eq. (3):

$$k' = \frac{\beta + k_e}{\beta + 1} \tag{3}$$

where k_e is the equilibrium segregation coefficient at any undercooling, β is the dimensionless velocity, defined as the following Eq. (4):

$$\beta = \frac{V}{D_i} \tag{4}$$

where V is the growth rate of interface, D_i is the diffusive speed of solute in the liquid. If the growth rate of interface (V) is much larger than the diffusive speed of solute in the liquid (D_i), then solute distribution coefficient of the moving solid–liquid phase interface (k') is considerably larger than the equilibrium segregation coefficient (k_e). Thus, a transition from equilibrium segregation to complete solute trapping occurs as the growth rate of interface surpasses the diffusive speed of solute in the liquid. The laser scanning speed adopted in this study is as high as thousands of millimeters per second resulting in a very high

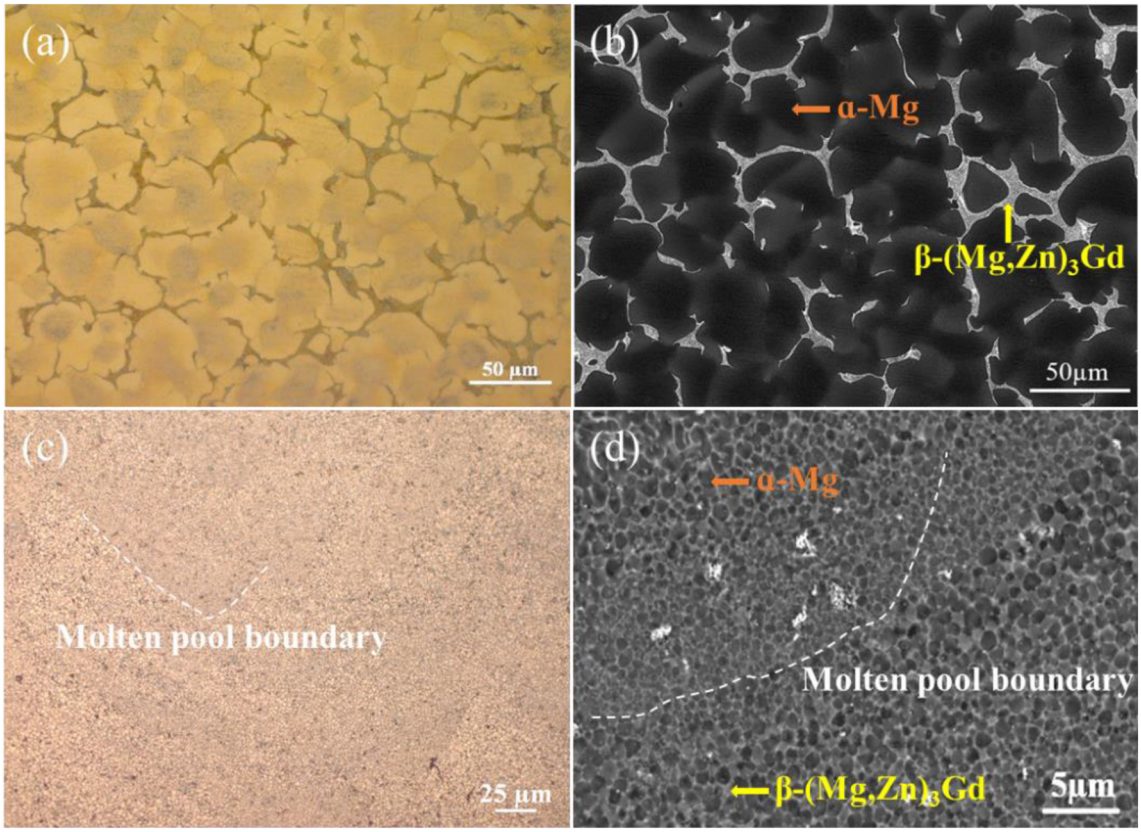

Fig. 7. OM (a, c) and (b, d) SEM images of semi-continuous as-cast alloy (a–b) and the SLMed GZ112K alloy (V = 300 mm/s, HS = 100 μm) from side view (c–d).

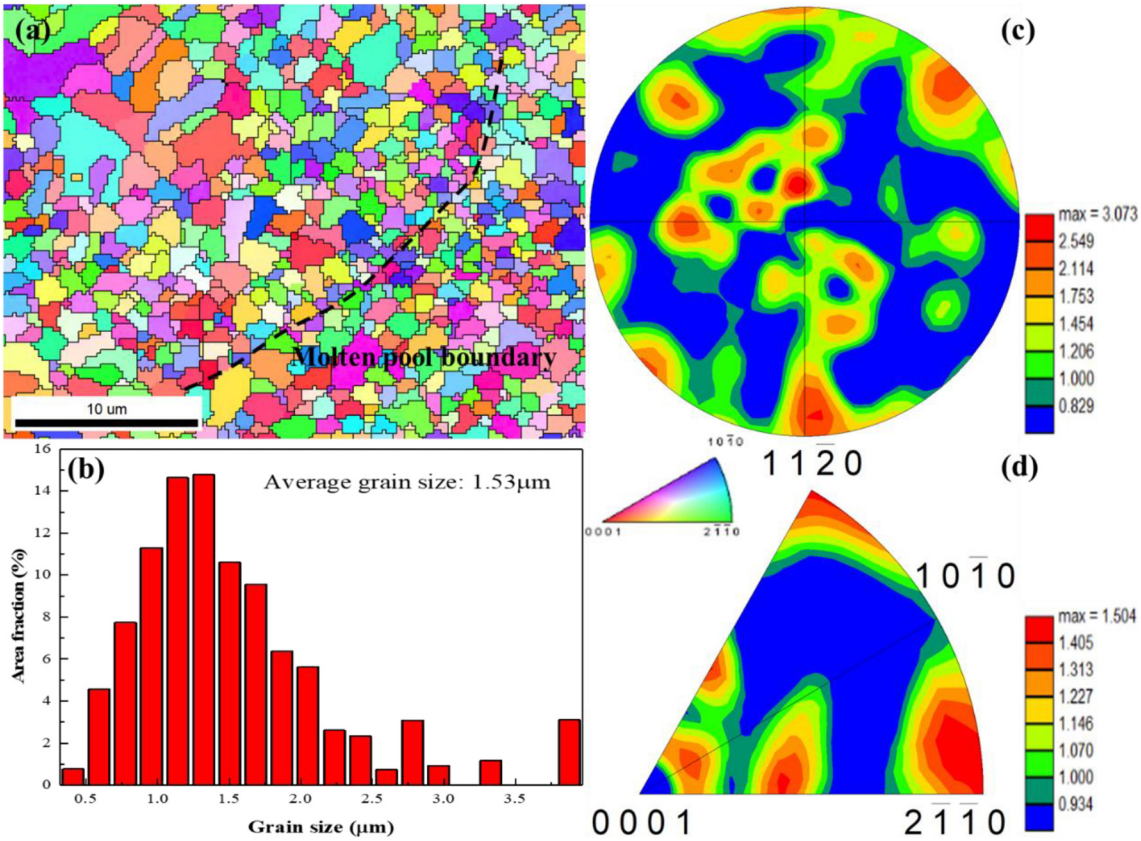

Fig. 8. The EBSD orientation map (a), grain size distribution (b), (0001) pole figures (c) and inverse pole figures (d) of the SLMed GZ112K alloy (V = 300 mm/s, HS = 100 μm).

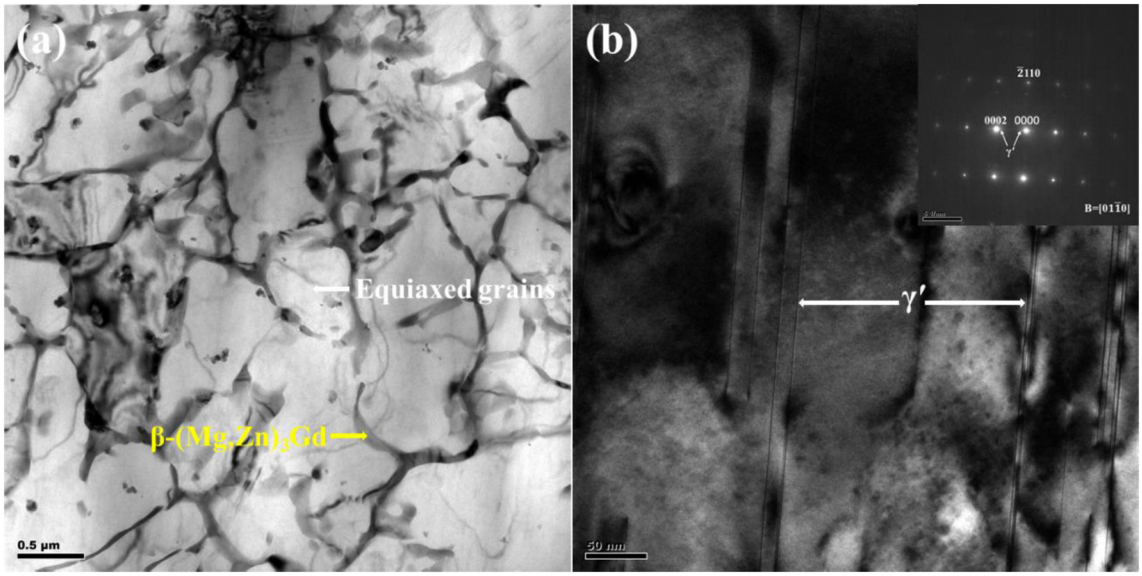

Fig. 9. Bright-field TEM micrographs and corresponding SAED patterns of SLMed GZ112K alloy (V = 300 mm/s, HS = 100 μm). The beams were parallel to the $[01\bar{1}0]_{\alpha}$ direction in (b).

growth rate of interface. Gd element do not have sufficient time for diffusion so that the effect of solute trapping appears in α-Mg matrix and therefore, the formation of Gd-rich β-$(Mg,Zn)_3Gd$ phase is suppressed to some extent. By increasing laser scanning speed from 100 mm/s to 1000 mm/s, the growth rate of interface also increases sharply. Therefore, k' is further larger than k_e and the effect of solute trapping is more significant leading to a smaller area fraction of eutectic β-$(Mg,Zn)_3Gd$ phase.

STEM/EDS was performed to identify the chemical composition in α-Mg matrix. Table 2 lists EDS results of α-Mg matrix of semi-continuous as-cast GZ112K alloy and SLMed GZ112K alloys at different scanning speeds. As for semi-continuous as-cast GZ112K alloy, most of Gd and Zn elements are distributed in the eutectic β-$(Mg,Zn)_3Gd$ phase. Therefore, the content of Gd and Zn elements in α-Mg matrix is only 5.15 ± 0.48 wt% and 0.79 ± 0.10 wt% respectively. However, the SLMed GZ112K alloy exhibits much higher content of Gd and Zn

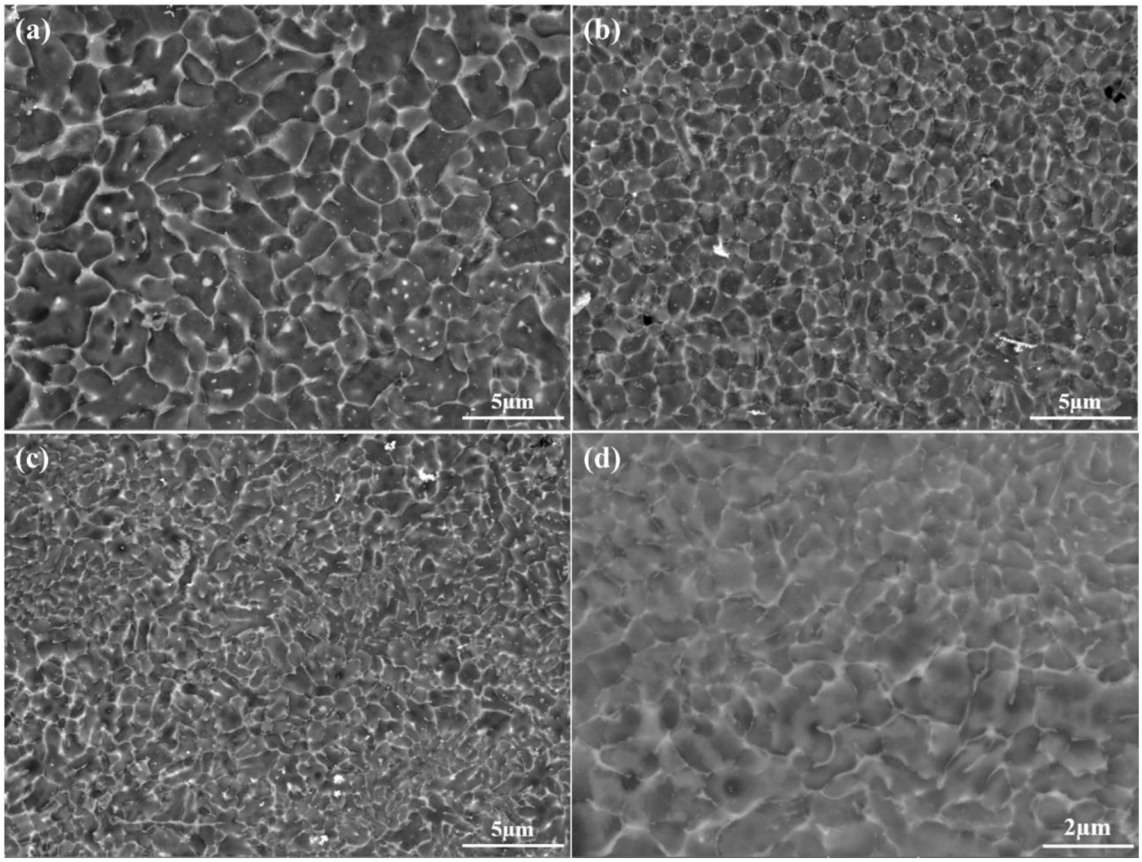

Fig. 10. SEM images of the SLMed GZ112K alloys at different scanning speeds: (a) V = 100 mm/s; (b) V = 500 mm/s; (c) V = 700 mm/s; (d) V = 1000 mm/s.

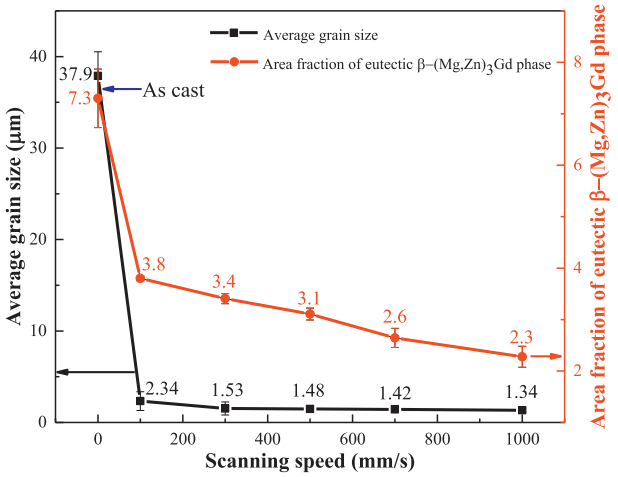

Fig. 11. Effect of laser scanning speed on average grain size and area fraction of eutectic β-$(Mg,Zn)_3Gd$ phase of the SLMed GZ112K alloys.

Table 2
EDS results from of α-Mg matrix of semi-continuous as-cast GZ112K alloy and SLMed GZ112K alloys at different scanning speeds.

Material	Gd (wt%)	Zn (wt%)	Mg (wt%)	Total (wt%)
As-cast	5.15 ± 0.48	0.79 ± 0.10	94.06 ± 0.49	100.00
SLMed-V100HS100	12.09 ± 0.14	1.43 ± 0.08	86.48 ± 0.16	100.00
SLMed-V300HS100	11.57 ± 0.19	1.49 ± 0.06	86.94 ± 0.20	100.00
SLMed-V500HS100	10.89 ± 0.17	1.58 ± 0.07	87.53 ± 0.18	100.00
SLMed-V700HS100	10.45 ± 0.18	1.61 ± 0.04	87.94 ± 0.18	100.00
SLMed-V1000HS100	10.06 ± 0.13	1.64 ± 0.03	88.30 ± 0.13	100.00

elements in α-Mg matrix (almost double), which will enhance both the effect of solid solution strengthening and corrosion resistances. Higher solid solubility of Gd and Zn elements in α-Mg matrix is consistent with lower content of eutectic phase (Fig. 11) in SLMed alloys. It could be observed that Gd content in α-Mg matrix decreases from 12.09 ± 0.14 wt% to 10.06 ± 0.13 wt% with increasing scanning speed. Although Zn content increases from 1.43 ± 0.08 wt% to 1.64 ± 0.03 wt% with increasing scanning speed, the Gd content is much higher than the Zn content, so the solid solution strengthening effect mainly comes from Gd element. Therefore, the solid solution strengthening effect of SLMed GZ112K alloys decreases with increasing scanning speed. Along with the increase in scanning speed, the effect of solute trapping becomes stronger leading to increased Gd content while element vaporization rate of Mg atoms reduces causing decreased Gd content. As result, under the interaction between the effect of solute trapping and element vaporization, Gd content in α-Mg matrix decreases with increasing scanning speed in spite of the fact that more proportions of Gd atoms are captured in α-Mg matrix.

3.4. Tensile properties

Fig. 12 shows room temperature tensile properties of the SLMed GZ112K alloy at different scanning speeds. Tensile properties of the as-cast alloy are also listed for comparison. As the laser scanning speed increases, the yield strength (YS) of the SLMed alloys decreases. Considering that there is no aging precipitate, the YS (σ_{YS}) of the SLMed alloys can be expressed by the following Eq. (5):

$$\sigma_{YS} = \sigma_0 + \sigma_{sp} + \sigma_{ss} + \sigma_{gb} \quad (5)$$

where σ_0 is the strength of pure Mg, σ_{sp} is the strength arising from secondary phase (eutectic β-$(Mg,Zn)_3Gd$ phase), σ_{ss} is the strength arising from the solute atoms, σ_{gb} is the strength arising from grain boundaries [45,46]. When scanning speed is 100 mm/s, the SLMed GZ112K alloy exhibits highest YS of 340 ± 6 MPa owing to strongest effect of solid solution strengthening in α-Mg matrix (σ_{ss} is the largest) although grains are a little coarser than those at other scanning speeds (σ_{gb} is the smallest). Besides, the area fraction of eutectic β-$(Mg,Zn)_3Gd$ phase at scanning speed of 100 mm/s is highest of all scanning speeds. The hardness and elastic modulus of eutectic phase is higher than α-Mg matrix [4] leading to the improvement of YS (σ_{sp} is the largest) but it may become the source of cracks during the deformation process and greatly reduce the plasticity of the alloy. However, a large number of pores in the sample cause stress concentration and high content of brittle eutectic phase, resulting in low elongation, and no effect of work hardening, resulting in no significant increase in ultimate tensile strength (UTS) compared with YS. When scanning speed is 1000 mm/s or 1500 mm/s, numerous lack of fusion defects due to low laser energy density lead to lower strength and ductility than as-cast GZ112K alloy.

The SLMed GZ112K alloys at scanning speed of 300–700 mm/s show the best tensile properties: both strength (YS and UTS) and ductility (elongation) are superior to those of as-cast GZ112K alloy due to the highest relative density of SLMed GZ112K samples in forming zones. As the laser scanning speed increases from 300 mm/s to 700 mm/s, the grain size drops a little bit (from 1.53 μm to 1.42 μm in Fig. 11) leading to the increment of σ_{gb}, but the area fraction of eutectic β-$(Mg,Zn)_3Gd$ phase (from 3.4% to 2.6% in Fig. 11) and the solid solubility of Gd atom in α-Mg matrix (from 11.57 wt% to 10.45 wt% in Table 2) decrease more resulting in the decrement of σ_{sp} and σ_{ss}. $\Delta\sigma_{gb} = kd_2^{-1/2} - kd_1^{-1/2}$, where k is termed stress intensity factor or

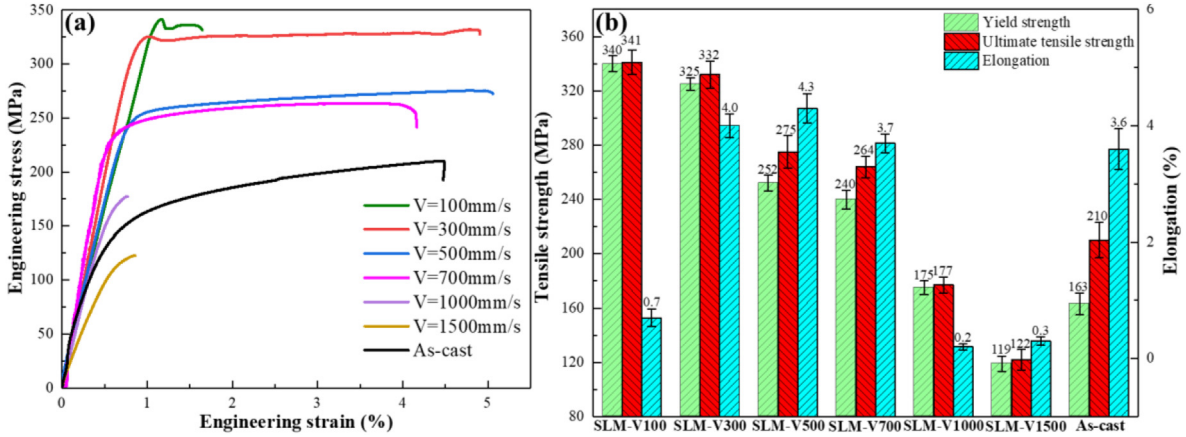

Fig. 12. Engineering stress-strain curves (a) and room-temperature tensile properties (b) of the SLMed GZ112K alloys at different scanning speeds (the hatch spacing is fixed at 100 μm) and as-cast alloy.

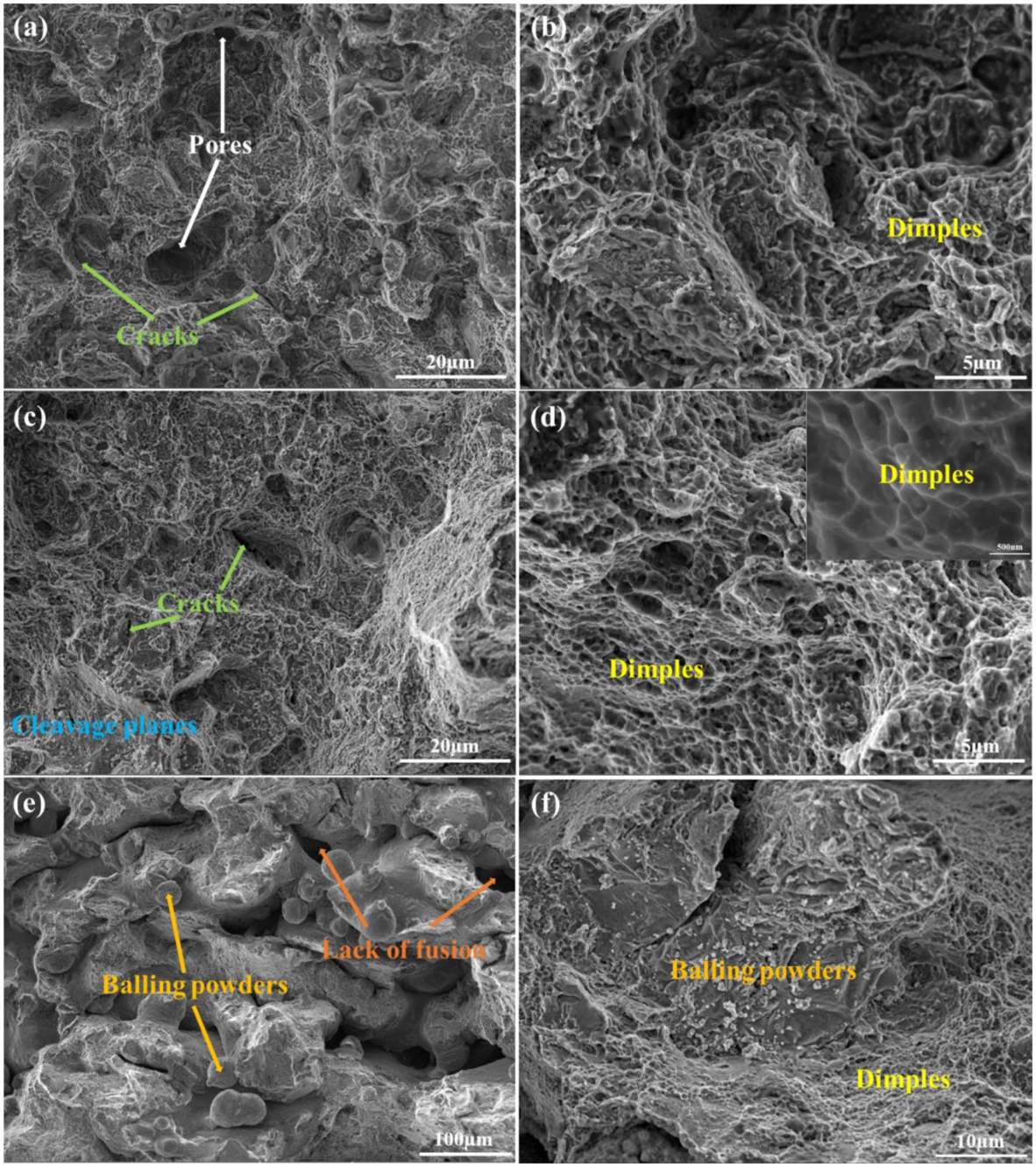

Fig. 13. Fracture morphologies of SLMed tensile samples at different scanning speed: (a–b) V = 100 mm/s; (c–d) V = 500 mm/s; (e–f) V = 1000 mm/s.

Hall-Petch slope (k = 280 MPa•μm$^{1/2}$), d_1 and d_2 are the average grain size (d_1 = 1.53 μm and d_2 = 1.42 μm). Substituting data as stated above, $\Delta\sigma_{gb}$ can be figured out ($\Delta\sigma_{gb}$ = 8.6 MPa). σ_{sp} and σ_{ss} contribute more to the total strength than σ_{gb}, so the YS of SLMed alloys decreases with increasing scanning speed from 300 mm/s to 700 mm/s. Besides, higher scanning speed can increase levels of residual stress [47], which is detrimental to the tensile properties. The SLMed GZ112K alloys at scanning speed of 300 mm/s exhibits optimal combination of strength and ductility: YS is 325 ± 5 MPa, UTS is 332 ± 10 MPa and elongation is 4.0 ± 0.2%. Compared with the as-cast alloy, the SLMed GZ112K alloy has obvious higher YS (+162 MPa) and UTS (+122 MPa) owing to significant fine grain strengthening (Fig. 11) and solid solution strengthening (Table 2) effect. Meanwhile, the SLMed GZ112K alloy shows comparable elongation (+0.4%) than the as-cast alloy, which is different from the lower elongation of the SLMed Mg-Al series alloys reported in other literatures [14,23,28]. Compared with other SLMed Mg alloys such as AZ91D [14], AZ61 [28], Mg-9wt%Al [23] and WE43 [15], the YS of 325 MPa in SLMed GZ112K alloy is highest. Besides, the YS of SLMed GZ112K alloy is even higher than extruded-T6/T5 Mg-11Gd-1Zn (wt%) alloy containing similar chemical compositions [48].

Fig. 13 shows the fracture morphologies of the SLMed tensile samples at different scanning speed. Although the fracture morphology of the SLMed tensile samples at scanning speed of 100 mm/s (Fig. 13a–b) is mainly composed of dimples, many pores cause premature fracture during the tensile test, resulting in lower elongation. The fracture morphology of the SLMed tensile samples at scanning speed of 500 mm/s (Fig. 13c–d) consists of many very small dimples (about 500 nm) with a small number of cleavage planes, indicating that the soft α-Mg matrix undergoes plastic deformation until it encounters the

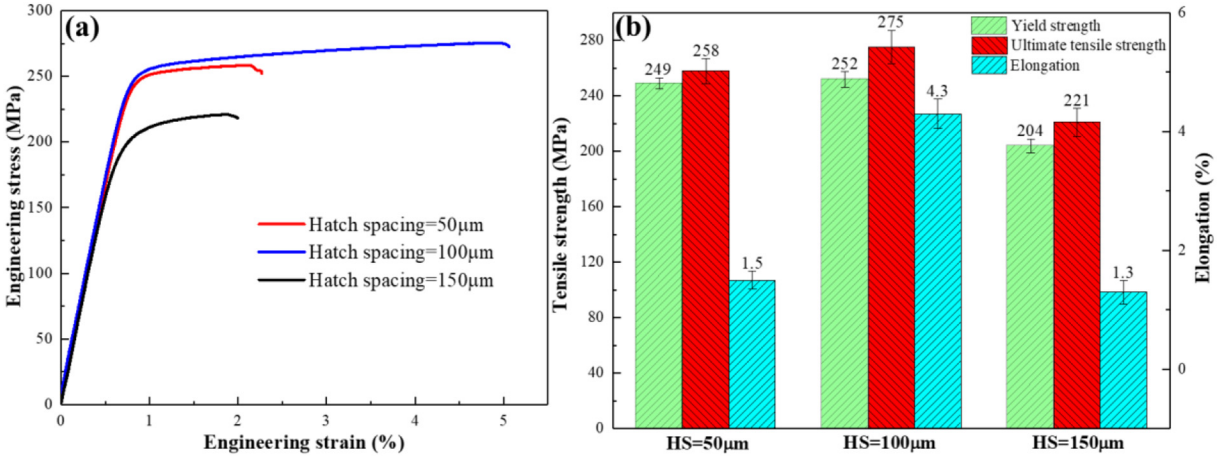

Fig. 14. Engineering stress-strain curves (a) and room-temperature tensile properties (b) of the SLMed GZ112K alloys at different hatch spacing (the scanning speed is fixed at 500 mm/s).

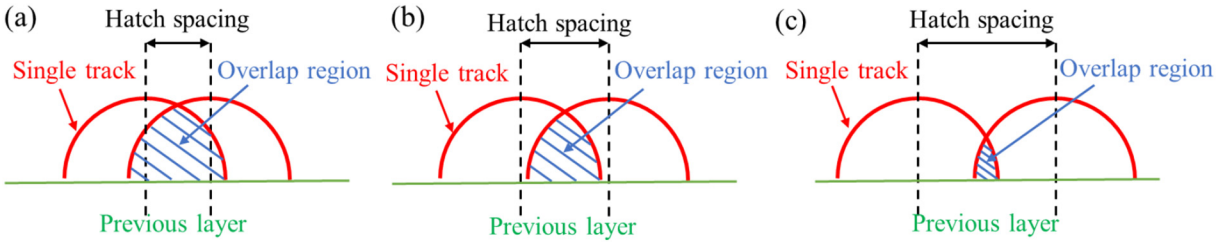

Fig. 15. Schematic diagram illustrating the effect of hatch spacing on area of overlap region: (a) low hatch spacing; (b) suitable hatch spacing; (c) high hatch spacing.

eutectic β-$(Mg,Zn)_3Gd$ phase on the grain boundary. As the laser scanning speed increases to 1000 mm/s, a large amount of balling powders and lack of fusion defects appear in the fracture (Fig. 13e–f), which is fatal to elongation. The balling effect often occurs at high scanning speed as a result of the Plateau–Rayleigh capillary instability of the molten pool [49].

Fig. 14 shows room temperature tensile properties of the SLMed GZ112K alloy at different hatch spacing. It can be easily found that SLMed GZ112K alloy at hatch spacing of 100 μm owns the best tensile properties: YS is 252 ± 6 MPa, UTS is 275 ± 12 MPa and elongation is 4.3 ± 0.3%. As shown in Fig. 15a, low hatch spacing leads to a larger area of overlap region, which causes more powder to be remelted to create more pores, resulting in much lower elongation. Besides, low hatch spacing will reduce processing efficiency of the SLM process. However, high hatch spacing is also detrimental to the SLM process. As shown in Fig. 15c, high hatch spacing reduces the height of the overlap region. After laying the next layer of powder, the thickness of the powder in the overlap region is larger than the thickness of the powder in the unlapped region, which may result in a large amount of lack of fusion defects in the overlap region because the laser cannot melt all the powder. It can be seen from Fig. 15b that suitable hatch spacing will make the height of the overlap region and the height of the unlapped region tend to be uniform, which will result in even powder distribution in the next layer. The overlap ratio (r) is defined as the ratio of the width of the overlap region to the width of the entire single track, which can be calculated by the following Eq. (6):

$$r = \frac{W_1}{W_2} = \frac{W_2 - HS}{W_2} = 1 - \frac{HS}{W_2} \tag{6}$$

where W_1 is the width of the overlap region, W_2 is the width of the entire single track and HS is hatch spacing. It can be seen from Fig. 4 that the width of the molten pool (corresponding to the width of the entire single track) is approximately 140 to 200 μm. When the hatch spacing is 100 μm, the corresponding overlap ratio is about 30–50%. Both excessively high and too low overlap ratio adversely affect the SLM process.

Combining the results of Figs. 3–5, 12–15, the optimum processing parameters of GZ112K alloy at a constant laser power of 80 W can be obtained: scanning speed is 300–700 mm/s and hatch spacing is 100 μm. Under the above optimum processing parameters, the SLMed GZ112K alloys not only have the fewest defects (pores and lack of fusion), but also exhibit excellent tensile properties.

4. Conclusions

High performance GZ112K alloy has been fabricated by selective laser melting technique in this study. Effect of processing parameters on microstructures and tensile properties of the SLMed GZ112K alloy were systematically analyzed. The main conclusions are listed as follows:

(1) Process map can be divided into three zones according to laser volume energy density: high energy input zones, forming zones and low energy input zones. Element vaporization mainly targeted at Mg and Zn during the process of SLM.
(2) Compared with as-cast GZ112K alloy, the SLMed GZ112K alloys not only have finer grains and eutectic β-$(Mg,Zn)_3Gd$ phase, but also have higher solid solubility of Gd and Zn elements. As the laser scanning speed increases, the average grain size, the area fraction of eutectic β-$(Mg,Zn)_3Gd$ phase and the solid solution strengthening effect decrease.
(3) The optimum scanning speed and hatch spacing at laser power of 80 W are 300–700 mm/s and 100 μm respectively. The SLMed GZ112K alloy at optimum processing parameters shows the best tensile properties: YS is 325 ± 5 MPa, UTS is 332 ± 10 MPa and elongation is 4.0 ± 0.2%.

Declaration of competing interest

The authors declare that they have no known competing financial interests or personal relationships that could have appeared to influence the work reported in this paper.

Acknowledgement

This work was funded by the National Key Research and Development Program of China (No. 2016YFB0701201), the National Natural Science Foundation (No. 51771113, 51971130) and the United Fund of National Department of Education and Equipment Development (No. 6141A02033213).

References

[1] B.L. Mordike, T. Ebert, Magnesium properties—applications—potential, Mater. Sci. Eng. A 302 (2001) 37–45.
[2] Y. Zhang, Y. Wu, L. Peng, P. Fu, F. Huang, W. Ding, Microstructure evolution and mechanical properties of an ultra-high strength casting Mg–15.6Gd–1.8Ag–0.4Zr alloy, J. Alloys Compd. 615 (2014) 703–711.
[3] W. Rong, Y. Zhang, Y. Wu, Y. Chen, T. Tang, L. Peng, D. Li, Fabrication of high-strength Mg-Gd-Zn-Zr alloys via differential-thermal extrusion, Mater. Charact. 131 (2017) 380–387.
[4] Y. Du, Y. Wu, L. Peng, J. Chen, X. Zeng, W. Ding, Formation of lamellar phase with 18R-type LPSO structure in an as-cast $Mg_{96}Gd_3Zn_1$(at%) alloy, Mater. Lett. 169 (2016) 168–171.
[5] M. Qian, D.H. StJohn, M.T. Frost, Characteristic zirconium-rich coring structures in Mg–Zr alloys, Scr. Mater. 46 (2002) 649–654.
[6] W. Rong, Y. Wu, Y. Zhang, M. Sun, J. Chen, L. Peng, W. Ding, Characterization and strengthening effects of γ′ precipitates in a high-strength casting Mg-15Gd-1Zn-0.4Zr (wt.%) alloy, Mater. Charact. 126 (2017) 1–9.
[7] D. Wang, P. Fu, L. Peng, Y. Wang, W. Ding, Development of high strength sand cast Mg–Gd–Zn alloy by co-precipitation of the prismatic β′ and β_1 phases, Mater. Charact. 153 (2019) 157–168.
[8] J.P. Weiler, A review of magnesium die-castings for closure applications, J. Magnes. Alloys 7 (2019) 297–304.
[9] J. Li, Z. He, P. Fu, Y. Wu, L. Peng, W. Ding, Heat treatment and mechanical properties of a high-strength cast Mg–Gd–Zn alloy, Mater. Sci. Eng. A 651 (2016) 745–752.
[10] S. Gangireddy, B. Gwalani, K. Liu, E.J. Faierson, R.S. Mishra, Microstructure and mechanical behavior of an additive manufactured (AM) WE43-Mg alloy, Addit. Manuf. 26 (2019) 53–64.
[11] K.G. Prashanth, S. Scudino, H.J. Klauss, K.B. Surreddi, L. Löber, Z. Wang, A.K. Chaubey, U. Kühn, J. Eckert, Microstructure and mechanical properties of Al–12Si produced by selective laser melting: effect of heat treatment, Mater. Sci. Eng. A 590 (2014) 153–160.
[12] G. Nussbaum, P. Sainfort, G. Regazzoni, H. Gjestland, Strengthening mechanisms in the rapidly solidified AZ 91 magnesium alloy, Scr. Metall. 23 (1989) 1079–1084.
[13] C.C. Ng, M.M. Savalani, M.L. Lau, H.C. Man, Microstructure and mechanical properties of selective laser melted magnesium, Appl. Surf. Sci. 257 (2011) 7447–7454.
[14] K. Wei, M. Gao, Z. Wang, X. Zeng, Effect of energy input on formability, microstructure and mechanical properties of selective laser melted AZ91D magnesium alloy, Mater. Sci. Eng. A 611 (2014) 212–222.
[15] N.A. Zumdick, L. Jauer, L.C. Kersting, T.N. Kutz, J.H. Schleifenbaum, D. Zander, Additive manufactured WE43 magnesium: a comparative study of the microstructure and mechanical properties with those of powder extruded and as-cast WE43, Mater. Charact. 147 (2019) 384–397.
[16] A.T. Polonsky, W.C. Lenthe, M.P. Echlin, V. Livescu, G.T. Gray, T.M. Pollock, Solidification-driven orientation gradients in additively manufactured stainless steel, Acta Mater. 183 (2020) 249–260.
[17] T. Vilaro, C. Colin, J.D. Bartout, L. Nazé, M. Sennour, Microstructural and mechanical approaches of the selective laser melting process applied to a nickel-base superalloy, Mater. Sci. Eng. A 534 (2012) 446–451.
[18] L. Thijs, F. Verhaeghe, T. Craeghs, J.V. Humbeeck, J.-P. Kruth, A study of the microstructural evolution during selective laser melting of Ti–6Al–4V, Acta Mater. 58 (2010) 3303–3312.
[19] R. Li, H. Chen, H. Zhu, M. Wang, C. Chen, T. Yuan, Effect of aging treatment on the microstructure and mechanical properties of Al-3.02Mg-0.2Sc-0.1Zr alloy printed by selective laser melting, Mater. Des. 168 (2019) 107668.
[20] M. Salehi, S. Maleksaeedi, H. Farnoush, M.L.S. Nai, G.K. Meenashisundaram, M. Gupta, An investigation into interaction between magnesium powder and Ar gas: implications for selective laser melting of magnesium, Powder Technol. 333 (2018) 252–261.
[21] D. Hu, Y. Wang, D. Zhang, L. Hao, J. Jiang, Z. Li, Y. Chen, Experimental investigation on selective laser melting of bulk net-shape pure magnesium, Mater. Manuf. Process. 30 (2015) 1298–1304.
[22] B. Zhang, H. Liao, C. Coddet, Effects of processing parameters on properties of selective laser melting Mg–9%Al powder mixture, Mater.Des. 34 (2012) 753–758.
[23] X. Niu, H. Shen, J. Fu, Microstructure and mechanical properties of selective laser melted Mg-9 wt%Al powder mixture, Mater. Lett. 221 (2018) 4–7.
[24] D. Schmid, J. Renza, M.F. Zaeh, J. Glasschroeder, Process influences on laser-beam melting of the magnesium alloy AZ91, Phys. Procedia 83 (2016) 927–936.
[25] A. Pawlak, M. Rosienkiewicz, E. Chlebus, Design of experiments approach in AZ31 powder selective laser melting process optimization, Arch. Civ. Mech. Eng. 17 (2017) 9–18.
[26] C. Taltavull, A.J. López, B. Torres, J. Rams, Fracture behaviour of a magnesium–aluminium alloy treated by selective laser surface melting treatment, Mater. Des. 55 (2014) 361–365.
[27] C. He, S. Bin, P. Wu, C. Gao, P. Feng, Y. Yang, L. Liu, Y. Zhou, M. Zhao, S. Yang, C. Shuai, Microstructure evolution and biodegradation behavior of laser rapid solidified Mg–Al–Zn alloy, Metals 7 (2017) 105.
[28] S. Liu, W. Yang, X. Shi, B. Li, S. Duan, H. Guo, J. Guo, Influence of laser process parameters on the densification, microstructure, and mechanical properties of a selective laser melted AZ61 magnesium alloy, J. Alloys Compd. 808 (2019) 151160.
[29] C. Shuai, L. Liu, M. Zhao, P. Feng, Y. Yang, W. Guo, C. Gao, F. Yuan, Microstructure, biodegradation, antibacterial and mechanical properties of ZK60-Cu alloys prepared by selective laser melting technique, J. Mater. Sci. Technol. 34 (2018) 1944–1952.
[30] K. Wei, Z. Wang, X. Zeng, Influence of element vaporization on formability, composition, microstructure, and mechanical performance of the selective laser melted Mg–Zn–Zr components, Mater. Lett. 156 (2015) 187–190.
[31] M. Zhang, C. Chen, C. Liu, S. Wang, Study on porous Mg-Zn-Zr ZK61 alloys produced by laser additive manufacturing, Metals 8 (2018) 635.
[32] K. Wei, X. Zeng, Z. Wang, J. Deng, M. Liu, G. Huang, X. Yuan, Selective laser melting of Mg-Zn binary alloys effects of Zn content on densification behavior, microstructure, and mechanical property, Mater. Sci. Eng. A 756 (2019) 226–236.
[33] C. Liu, M. Zhang, C. Chen, Effect of laser processing parameters on porosity, microstructure and mechanical properties of porous Mg-Ca alloys produced by laser additive manufacturing, Mater. Sci. Eng. A 703 (2017) 359–371.
[34] L. Thijs, K. Kempen, J.-P. Kruth, J. Van Humbeeck, Fine-structured aluminium products with controllable texture by selective laser melting of pre-alloyed AlSi10Mg powder, Acta Mater. 61 (2013) 1809–1819.
[35] K. Guan, Z. Wang, M. Gao, X. Li, X. Zeng, Effects of processing parameters on tensile properties of selective laser melted 304 stainless steel, Mater.Des. 50 (2013) 581–586.
[36] T. Guraya, S. Singamneni, Z.W. Chen, Microstructure formed during selective laser melting of IN738LC in keyhole mode, J. Alloys Compd. 792 (2019) 151–160.
[37] A. Block-Bolten, T.W. Eagar, Metal vaporization from weld pools, Metall. Mater. Trans. B Process Metall. Mater. Process. Sci. 15B (1984) 461–469.
[38] X. Zeng, Y. Wang, W. Ding, A.A. Luo, A.K. Sachdev, Effect of strontium on the microstructure, mechanical properties, and fracture behavior of AZ31 magnesium alloy, Metall. Mater. Trans. A 37A (2006) 1333–1341.
[39] D.H. StJohn, M. Qian, M.A. Easton, P. Cao, The interdependence theory: the relationship between grain formation and nucleant selection, Acta Mater. 59 (2011) 4907–4921.
[40] D. Zhang, D. Qiu, M.A. Gibson, Y. Zheng, H.L. Fraser, D.H. StJohn, M.A. Easton, Additive manufacturing of ultrafine-grained high-strength titanium alloys, Nature 576 (2019) 91–95.
[41] Y. Ali, D. Qiu, B. Jiang, F. Pan, M.-X. Zhang, Current research progress in grain refinement of cast magnesium alloys: a review article, J. Alloys Compd. 619 (2015) 639–651.
[42] J.F. Nie, K. Oh-ishi, X. Gao, K. Hono, Solute segregation and precipitation in a creep-resistant Mg–Gd–Zn alloy, Acta Mater. 56 (2008) 6061–6076.
[43] Y.J. Wu, D.L. Lin, X.Q. Zeng, L.M. Peng, W.J. Ding, Formation of a lamellar 14H-type long period stacking ordered structure in an as-cast Mg–Gd–Zn–Zr alloy, J. Mater. Sci. 44 (2009) 1607–1612.
[44] M.J. Aziz, Model for solute redistribution during rapid solidification, J. Appl. Phys. 53 (1982) 1158–1168.
[45] Z.-Z. Jin, M. Zha, Z.-Y. Yu, P.-K. Ma, Y.-K. Li, J.-M. Liu, H.-L. Jia, H.-Y. Wang, Exploring the Hall-Petch relation and strengthening mechanism of bimodal-grained Mg–Al–Zn alloys, J. Alloys Compd. 833 (2020) 155004.
[46] D. Qiu, M.-X. Zhang, Strengthening mechanisms and their superposition law in an age-hardenable Mg-10 wt pct Y alloy, Metall. Mater. Trans. A 43 (2012) 3314–3324.
[47] N.C. Levkulich, S.L. Semiatin, J.E. Gockel, J.R. Middendorf, A.T. DeWald, N.W. Klingbeil, The effect of process parameters on residual stress evolution and distortion in the laser powder bed fusion of Ti-6Al-4V, Addit. Manuf. 28 (2019) 475–484.
[48] R. Zhen, Y. Sun, F. Xue, J. Sun, J. Bai, Effect of heat treatment on the microstructures and mechanical properties of the extruded Mg–11Gd–1Zn alloy, J. Alloys Compd. 550 (2013) 273–278.
[49] A.V. Gusarov, I. Yadroitsev, P. Bertrand, I. Smurov, Heat transfer modelling and stability analysis of selective laser melting, Appl. Surf. Sci. 254 (2007) 975–979.